Capillary interaction in wet granular assemblies: Part 2

Falk K. Wittel, Roman Mani, Konstantin Melnikov, Filippo Bianchi, and Hans J. Herrmann

Abstract This chapter focuses on Discrete Element models using Contact Dynamics, that capture the behavior of granular assemblies with fluid on the pore scale. The effect of the timescales, introduced by the fluid transport on relaxation, fluid migration, and failure are identified and studied in particle simulations and accompanying experiments. To extend the simulation capabilities to larger fluid contents, a discretization scheme for arbitrary liquid bodies with morphological evolution laws is employed, that combines experimental observations and results from small-scale Numerical Energy Minimization (NEM) simulations (part 1). We demonstrate that this way, fluid saturation in random packings can be simulated with arbitrary liquid contents ranging from dry to full saturation with good accuracy.

Institute for Building Materials
ETH Zurich
Stefano-Franscini Platz 3
CH-8093 Zurich
Tel.: +41 44 633 2871
e-mail: fwittel@ethz.ch

Nomenclature

α_{jk}	opening angle
β	opening angle
ε	geometrical correction parameter
η	fluid viscosity
η^{coh}	cohesion number
γ	shear deformation
γ	surface tension
κ	inverse flow resistance
λ	drainage parameter
μ	Coulomb friction coefficient
μ_f	internal friction coefficient
ω_{ij}	conductance coefficient
Φ	packing density
ϕ	face-edge angle of tetrahedron
ψ	filling angle of the meniscus
σ	stress
τ	shear strength
τ_i	relaxation times
θ	angle of internal friction
θ	contact angle
ε	strain
A	area
a_i, b	fitting parameters
C	surface curvature
c	cohesion
D	macroscopic diffusion constant
F	force
g_{ij}	local conductance coefficient between two pores
H	height
N	number
P	pressure

q	differential stress
Q_{eff}	net in- or outflow from a cell
q_{ij}	liquid flux between neighboring cells i, j
R	particle radius
$r_{1,2,men}$	radii of curvature of bridges $(_{1,2})$ and menisci $(_{men})$
$s_{ij/c}$	particle distance / bridge rupture distance
t	time
V	volume
V_{ij}	volume of liquid bridge between particle i and j
W_c	liquid volume content
x, y, z	Cartesian coordinates
CD	Contact Dynamics
DEM	Discrete Element Method
NEM	Numerical Energy Minimization
pbc	periodic boundary condition
v	velocity

1 Introduction

Liquids are known to alter the mechanical behavior of granular systems dramatically what can be impressively experienced when creating sculptures such as the one shown in Fig. 1, that can only defy gravity as long as the sand is wet and partially saturated [25]. Cohesion by capillary forces, acting between neighboring grains, gives loose sand tensile strength. Increasing computer power allows to quantitatively study the nature of this phenomenon on the scale of single grains - also called pore scale - experimentally by computer tomography (part 1) and numerically on representative assemblies (part 2). These findings help to understand the processing of wet granulates, for example for granulation, molding or transport in the pharmaceutical industry, in materials or food processing.

Fig. 1 ETH main building by ETH Prof. Gottfied Semper (1864) carved in sand (unknown artist from the 2017 AIV student sandcastle competition).

For wet granular matter, one typically distinguishes four different states, characterized by increasing saturation: *pendular, funicular, capillary* and *slurry* [26, 45]. The *pendular state* is characterized by the sole existence of liquid bridges between grain pairs. The Laplace pressure of the liquid phase is negative resulting in attractive inter-granular forces. If more fluid is available, the *funicular state* is reached, where liquid bridges and fully saturated pores coexist, that still exert attractive forces. The *capillary state* is reached when liquid fills almost all pores. Note that still concave menisci exist, resulting in a net cohesive force on the grain assembly. This condition distinguishes it from the *slurry state*, where the Laplace pressure in the liquid phase is equal to or larger than the air pressure. Without cohesion, the real material behavior is similar to the completely dry state [23]. On a geotechnical scale, landslides and debris flow are prominent examples of slurries, which are dangerous natural hazards occurring mostly in mountainous terrain when heavy rainfall mobilizes a large amount of debris. The mechanical properties of the granular soil are significantly altered before slope failure by the increasing presence of water. After

cohesion reaches a maximum at lower saturation, capillary forces slowly decrease until the gravitational load exceeds cohesion and landslides can be triggered. This triggering effect can be studied by tracking the liquid distribution on the micro-scale. However, the complex nature of the problem requires larger assemblies of particles to be representative for the bulk. For larger liquid contents, also an astonishing richness of liquid body morphologies are revealed by computer tomography studies, which render direct computations based on surface minimization principles inapplicable. As we will show in the following, the findings from these simulations of Part 1 are valuable as direct input into grain scale models allowing to execute meaningful calculations on the microscopic level.

The organization of the chapter is as follows: Before focusing on models for wet granular assemblies, we demonstrate in Sec. 2 on two simple experimental setups the interplay of micro-scale forces, packing densities, liquid redistributions and resulting macro-behavior under tensile and shear loading. In Sec. 3 we describe model extensions to include the liquid into contact dynamics (CD) with spherical particles. After a brief description of CD, the essential phenomena and fundamental models for the pendular state are reviewed, and extensions to the funicular state are described. Sec. 4 starts with simulations of the pendular state where studies of fluid migration under shear are shown before the formation of liquid clusters and the loss of cohesion is studied for increasing liquid content.

2 Liquid in multi-grain assemblies

The mechanical behavior of granular packings is rather complicated. Liquids add complexity, as it introduces new timescales for fluid transport, depending on the transport mechanism. We demonstrate this for observations of force relaxation in a tensile split box setting and by liquid migration from shear bands in a shear cell.

2.1 Tensile behavior in the pendular state

The pendular state is characterized by the exclusive presence of liquid bridges. They form when two grains contact each other, start to act mechanically, once they overcome the effect of roughness [21], exchange fluid through the wetting film covering the particles [61] or the vapor phase [28] driven by Laplace pressure differences [55] and once excessively stretched, fracture [70]. Tensile failure of wet soils, for example, initiates landslides. Hence, it is important to understand the tensile stress relaxation in multi-grain assemblies as the cumulation of microscale forces and processes from capillary bridges, inter-particle friction, liquid flows and particle movements. We demonstrate the tensile relaxation behavior on a split cell box with rough inner surfaces (see Fig. 2(a)), filled by wet glass beads with mean radius of $\bar{R} = 61\mu$m, liquid volume content W_c below 2.4% and two distinct packing densities

$\Phi \approx 0.41, 0.51$ by loosely filling and compacting via vibration (full description in Ref. [3]). One half of the split cell is moved at a constant velocity of $4 \cdot 10^{-6}$m/s, while the reaction force is measured on the second. When during the first extension the global strength is reached at a displacement of about 1.5-2.3$\bar{r}$, the position is kept, and the system relaxes for 30 minutes before the test is proceeded until complete separation (see a typical test in Fig. 2(b)). To reveal the effect of surface tension γ, one set of experiments was done with water ($\gamma = 72.8$mN/m) and another with added surfactant ($\gamma = 32.8$mN/m).

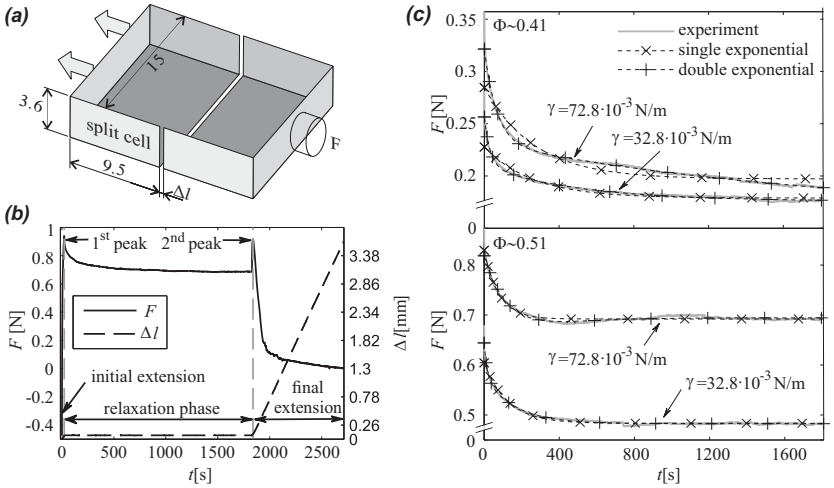

Fig. 2 (a) Split cell setup with dimensions in cm. (b) Prescribed displacement and reaction force for $\Phi \approx 0.51$ and $\gamma = 32.8$mN/m. (c) Force decay after stopping the initial extension for $\Phi = 0.41$ (top) and $\Phi = 0.51$ (bottom). (b,c) Reprint by permission from Springer Nature: Ref. [3].

.

As one expects, the mean force of the first peak is about 2.5 times higher for the higher packing fraction. In dense packings ($\Phi \approx 0.51$), strains above which a crack becomes visible are about one order of magnitude lower than in loose packings and close to the peak force, while for $\Phi \approx 0.41$, particle rearrangements prohibit an early detection of the crack. Those observations are in agreement with earlier works on tensile strength [9, 14, 19, 33, 39, 49, 50, 64]. The higher strength has to do with a larger number of liquid bridges and smaller inter-particle distances resulting in increased resistance for spatial rearrangement, since each particle displacement involves the mobilization of a larger number of particles [22]. Smaller surface tension results for both packing fractions in lower strength (see Fig. 2). Using particle sizes, liquid content and assuming a connectivity of 6 bridges per particles, one can estimate with Eq. 5 a rupture distance $s_c \approx 24\mu$m . Note that displacement values at the peak force for $\Phi = 0.51$ are around 90μm. The relaxation phase is characterized by a slowing down relaxation towards a steady state (see Figs. 2(c)) that can be fitted

by exponential decay functions in the time domain:

$$F = \sum_{i=1}^{2} a_i e^{-t/\tau_i} + b \tag{1}$$

with elapsed time t, relaxation times τ_i and fitting parameters a_i, b. Fits are shown in Fig. 2(c) revealing, that low packing fractions Φ require at least $i = 2$, while high Φ can be described already with single exponential functions. The distinct relaxation behavior of loose and close packing is not affected by surface tension γ, while strength clearly depends on γ. During the relaxation phase one expects three phenomena: (i) liquid bridge ruptures, (ii) fluid redistribution and (iii) grain rearrangements (see Fig.3 (b)). Fluid redistribution between capillary bridges occurs

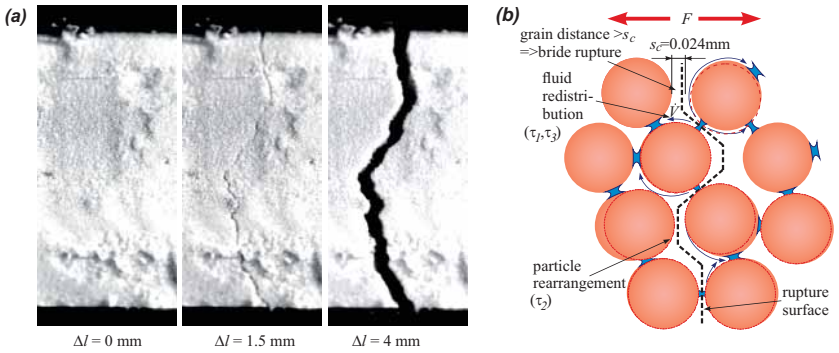

Fig. 3 (a) Fracture evolution $\Phi = 0.41$ and sketch of relaxation phenomena. Reprint by permission from Springer Nature: Ref. [3].

through the thin wetting film surrounding rough particles, driven by differences in the Laplace pressure [61] and through the vapor phase [29]. Extension or dilation of the packing elongates bridges, resulting in increasing Laplace pressure, reduced capillary force (Eq. 4) and consequently fluid flux into bridges with lower Laplace pressure until they equilibrate or rupture [30, 31, 32]. The local fluid depletion results in locally reduced internal stress, internal load redistributions, bridge ruptures and consequently particle rearrangements. Rearrangements themselves modify the capillary bridge network, resulting in pressure variations between liquid bridges, driving fluid flux, and so forth. The timescale for water redistribution is about 300 s [23] while the one of the grain rearrangement is shorter and between 20 and 300 s, following [22]. The observed relaxation times for the double exponential fits of the loose packings are $\tau_1 = 50$ s and $\tau_2 = 1200$ s, indicating the presence of two different phenomena dominating during relaxation - the fast grain rearrangement and the slower fluid redistribution. In the highly packed samples, the fluid redistribution dominates, since one single exponential function sufficiently describes relaxation and particle mobility. Higher packing results in increased connectivity [16, 28], thus

smaller bridge volumes and consequently faster fluid depletion and larger differences in Laplace pressure, hence shorter measured relaxation times ($\tau_1 \approx 145$ s).

2.2 Liquid migration from shear bands

The process of fluid depletion in regions with strain localization, described in Sec. 2.1 is relevant also in shear zones due to inherent dilation. To be able to observe fluid depletion, a stable shear band is realized in a circular split bottom cell [12], consisting of an outer L-shaped cylinder profile and an inner rotating cylinder with an attached disk, sketched in Fig. 4(a) (see also [37]). The shear cell is filled up to 15 mm with glass beads (radii R=0.85±0.075 mm) and the homogeneously distributed liquid (1%) is fluorescent UV glue ($\gamma = 40$ mN/m; $\theta = 10°$; viscosity $\eta = 300$ mPa·s) and hardens quickly when irradiated with UV light. After shearing by rotating eight times with 10 minutes per rotation, the glue is quickly hardened and thus stores the liquid configurations for subsequent evaluation. The entire pore space of the granulate is filled with colorless epoxy resin to obtain a solid block to be able to cut 3 mm thick cross sections that are suitable for fluorescent imaging under UV-light (see Fig. 4(b)).

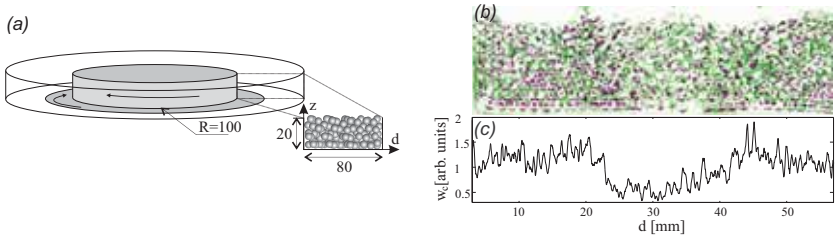

Fig. 4 (a) Circular split bottom shear cell with rotating core (gray) and units in mm. (b) 3 mm thick slice with liquid bridges (magenta) and particles (green), showing the fluid migration away from the shear band forming at about $d = 30$ mm. (c) Averaged spatial distribution of liquid content W_c in the cross section. Reprint by permission of APS: Ref. [37].

It is evident from Fig. 4, that liquid is driven out of the shear band and accumulates towards the edges. Fig. 4(c) shows the liquid content as a function of the distance d from the outer fixed cylinder wall averaged over heights $z > 3.4$ mm. The liquid content was evaluated by summing the pixels that belong to a liquid bridge and averaging over eight cross sections. Liquid depletion in the shear band could, in fact, be a cause for the shear softening behavior of wet granular systems. However, these observations are only valid in the pendular state up to a liquid content $W_c^{max} \leq 2.4\%$ where only liquid bridges form. To be able to understand and generalize such findings, suitable models for wet particle assemblies and simulations, described in the following are required.

3 Discrete Element models for granular assemblies with capillary interactions

Simulations of the mechanical behavior of unsaturated granular systems are rather straightforward, as long as particles only experience inter-particle contact forces, Coulombian friction, and cohesive forces from liquid bridges in the pendular state. For increased liquid content, however, a richness of higher order liquid morphologies arises which continuously change due to deformation of the solid phase. In any case, to simulate the behavior of a granular system, Newton's equations of motion have to be integrated for the entire grain assembly to follow its time evolution [24]. The problem can be solved either explicitly, allowing particle overlap for contact force calculations [11], or implicitly using contact dynamics (CD) [46]. The first one is the method of choice when elastic deformations, represented via grain overlap, are relevant and contact interactions need to be resolved by tiny time steps. However, for perfectly rigid, frictional particle systems at high packing fractions but negligible particle elasticity, the contact dynamics method can be superior [27]. Implicit calculations of contact forces with the zero overlap constraint result in a high dimensional system of equations that require a solution at each time step. The substantially increased computational cost, however, is more than counteracted by several orders of magnitude larger time increments. In the following first CD is explained, before we describe extensions of the method to account for liquid bridges and finally arbitrary liquid bodies.

3.1 Contact dynamics in a nutshell

Contact Dynamics (CD), originally proposed by Moreau [46] is based on the assumption of perfectly rigid, frictional particles. In such systems, exclusively the rearrangements of particles determine the system's behavior [6]. Like other discrete element methods, CD calculates the trajectory of each particle and its rotation. A force F^p acts on each particle, that is composed of the contact forces F_i^c with all $i = 1...n$ contacting particles and boundaries like walls, a gravitational force F^v, as well as forces from the liquid (see Sec. 3.3.1). In CD a strict volume exclusion constraint is implemented, and the normal force component F^n can take arbitrary large positive values if the particle distance between surfaces of particles s_{ij} becomes zero, unless there is cohesion, to avoid surface interpenetration. Consequently, one must determine the position of the particle in an iterative process for which the F^n of each active contact is minimal such that there is no overlap of particles at the next time step. When $s_{ij} > 0$, the corresponding F^n vanishes, unless attractive cohesive forces F^{coh} act in the normal direction, e.g., in a range $0 < s_{ij} < s_c$. Sliding at particle contacts is prevented if the tangential component of the contact force F^t is smaller than the threshold determined by the Coulomb friction coefficient μ: $0 \leq F^t \leq \mu F^n$

(see Fig.5), with equal values for the static and dynamic friction coefficients. F^t introduces a moment around the particle center resulting in particle rotation.

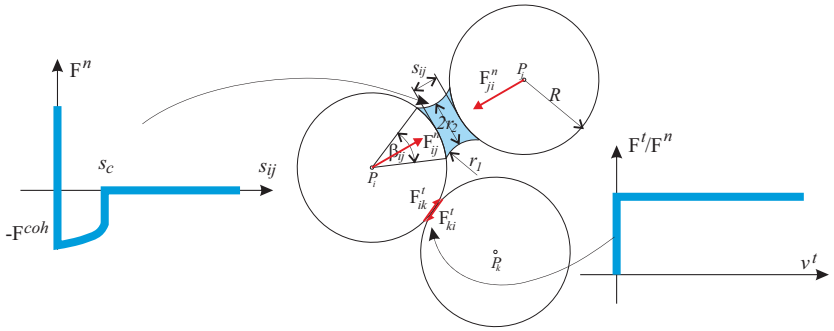

Fig. 5 Contact laws in CD with different particle configurations (center). (left) Repulsive normal force F^n with volume exclusion constraint for $s_{ij} = 0$ and attractive cohesive force F^{coh} with rupture distance s_c. (right) Sticking until tangential force $F^t < \mu F^n$. Reprint of central drawing by permission from Springer Nature: Ref. [43].

In dense packings, particles typically interact through a contact force network. Hence, a system of equations must be solved, e.g., by an iterative algorithm on all particles in a random order to obtain the global solution of contact forces [6]. The global contact force network converges iteratively toward a relaxed state providing the required forces for the integration of the equations of motion by an implicit Euler method.

3.2 Models for granular assemblies in the pendular state

Molecules of a liquid attract each other. However, at surfaces with a gaseous phase, the number of cohesive interaction partners of the same kind differs from inside the bulk, where molecules are equally pulled in all directions by their neighbors. Molecules at the surface experience a net force which is directed normal to the surface, resulting in surface tension γ or energy [69]. γ denotes the increase in free energy per unit surface area required to bring molecules from the bulk to the surface. Since interface molecules are in an energetically unfavorable state, the liquid tries to minimize its surface. As a consequence, a pressure jump ΔP occurs by passing across the interface, called Laplace pressure. For convex liquid surfaces like droplets, the pressure inside is larger (overpressure), while for concave interfaces, common for unsaturated porous media, it is negative. The Young-Laplace equation connects the geometry via surface curvature C and surface tension γ to the pressure difference ΔP:

$$\Delta P = \gamma C = \gamma(r_1^{-1} + r_2^{-1}), \tag{2}$$

where $r_{1,2}$ are the principal radii of curvature. With increasing curvature C, ΔP increases linearly. A Euler-Lagrange formalism is used for the minimization of the surface under the condition of volume conservation [69] as demonstrated in Part 1 of this work.

When a liquid drop sits on a solid, the liquid-gas interface will touch the solid at a certain contact angle along the so-called wetting or triple line. The Young-Dupré equation describes the relation between the surface tensions of the three phases liquid (L), solid (S) and gas (G) in equilibrium: $\gamma_{SG} - \gamma_{SL} = \gamma_{LG} \cdot \cos\theta$ with the contact angle $\theta = 0°$ for complete wetting, $0° < \theta < 180°$ for partial wetting and $\theta = 180°$ for non-wetting situations [4, 15]. Note that on rough surfaces, measured contact angles can differ from the value predicted by the Young-Dupré equation. If the volume of a stable liquid body is increasing, the wetting line will advance once the advancing contact angle θ_A is reached. Vice-versa, volume reduction only results in a receding wetting line when reaching the receding contact angle θ_R [15]. The experimentally observed contact angles θ will be in the range $\theta_A \leq \theta \leq \theta_R$, depending on the history of the system and the difference $\theta_A - \theta_R$ is called contact angle hysteresis and has multiple practical implications in agitated granular packings at low saturation states [35, 38].

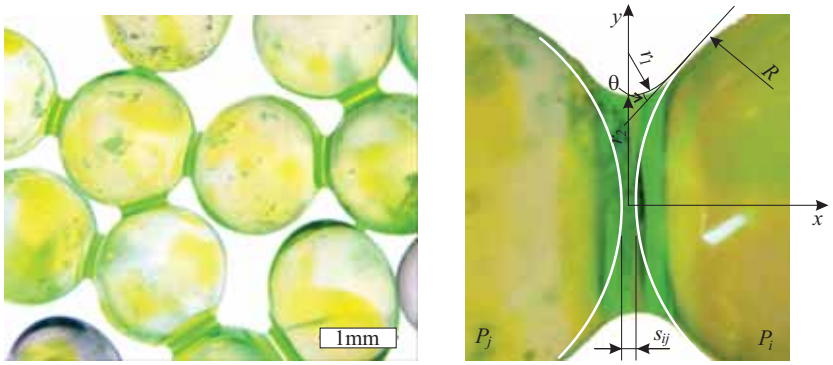

Fig. 6 Fluorescence microscope image for a partially saturated packing of glass beads in the pendular state and a single capillary bridge between two particles.

The presence of a liquid phase adds additional forces to particles connected by liquid bridges. These bridges form at contact points as soon as particles touch. No matter whether liquid is located in the wetting layer on a rough grain surface or in bridges, the total liquid volume must be conserved. At lower saturation, liquid bridges like the ones in Fig. 6 are the elementary units and dominantly observed basic liquid structure in the pendular state. Due to its relative simplicity, the pendular state received substantial attention by experimentalists and theoreticians alike, who

developed approximate solutions. For small grains the effect of gravity on the shape of liquid bridges is negligible. The resulting rotational symmetry of the structure with respect to the line connecting the grain centers is an important simplification for the solution of the Young-Laplace equation (Eq. 2)

$$\Delta P = \gamma \left(\frac{\ddot{y}(x)}{(1+\dot{y}(x)^2)^{3/2}} - \frac{1}{y(x)(1+\dot{y}(x)^2)^{1/2}} \right), \tag{3}$$

where $y(x)$ describes the liquid-gas interface of the bridge in the $x-y$ plane shown in Fig. 6 [32]. Various suggestions were made for solving $y(x)$ with increasing accuracy. The toroidal approximation proposed by Ref. [14] describes $y(x)$ by a circular arc with constant radii $r_{1,2}$. This leads through Eq. 3 to an analytical relation of ΔP as a function of the separation s_{ij}, the contact angle θ and the bridge volume V_{ij}. Unfortunately the assumption $r_1 = const$ is unrealistic (see for example Fig. 6(b)) and one needs to solve Eq. 3 numerically with the boundary condition given by the contact angle θ as shown in Refs. [32, 58].

If ΔP is known, the attractive capillary force F_{ij}^{cap} can be calculated. It consists of two components: the forces $F_\gamma = 2\pi y(x)\gamma$ due to the surface tension acting on the profile $y(x)$ and $F_{\Delta P} = \pi y(x)^2 \Delta P$ due to the pressure drop ΔP [32]. Since F_{ij}^{cap} must be independent of the x-position one can evaluate it at the neck [45] and obtains $F_{ij}^{cap} = F_\gamma + F_{\Delta P} = 2\pi y(0)\gamma + \pi y(0)^2 \Delta P$. A closed form expression for the force acting between particles i and j of equal radius R was derived by [70]:

$$F_{ij}^{cap} = \frac{4\pi R\gamma \cos\theta}{2 + s_{ij}\sqrt{R/V_{ij}} + 5s_{ij}^2 R/V_{ij}}. \tag{4}$$

It is important to note that Eq. 4 is only valid for small capillary bridges up to $V \approx 0.03R^3$. It also gives a constant force, independent from V_{ij} at grain contact ($s_{ij} = 0$) contrary to real bridges. Due to particle roughness, the full capillary force F_{ij}^{cap} only acts above a threshold volume V_c. This can be considered using a Heaviside step function to switch on F_{ij}^{cap} when the volume reaches V_c [36]. From there on the respective capillary force F_{ij}^{cap} is calculated by the empirical relation Eq. 4 until the bridge ruptures by fulfilling the criterion described in Eq. 5. Additionally, real bridges can only be stretched to a volume dependent rupture distance s_c. Based on experimental observations, Willett *et al.* [70] proposed a refined expression with higher order terms to obtain the criterion for bridge rupture as

$$s_c \geq (1+\theta/2)(V_{ij}^{1/3} + 0.1V_{ij}^{2/3}). \tag{5}$$

Fluid redistributes in wet particle systems in various ways. First, in the case of *bridge ruptures* the fluid that once was in the bridge is sucked back into the wetting layers of the two involved grains [61]. The larger one of the grains is with respect to the other, the larger fraction of water it will receive and the liquid portions can be estimated via a scheme described in Ref. [63]. Since the wetting film swells, its flow resistance drops and fluid gets quickly sucked into already existing bridges,

because their Laplace pressures are low compared to the wetting layer. In the models, one can equally redistribute the fluid on the particle to all intact bridges of that particle [36], distribute it proportional to the pressure differences between individual Laplace pressures P_i and the film pressure $P_f = \gamma/R$ or inversely proportional to the distance of a bridge from the rupture point of the failed bridge L_i. Mani *et al.* [37] proposed a combination where the amount of liquid each bridge receives is $\Delta V_i = A(P_f - P_i)/L_i$ with the normalization factor A to assure volume conservation. Timescales for bridge failure and redistribution can be considered to be of the same order, and for slow loading, assuming instantaneous redistribution is sufficient. Due to liquid redistribution from bridge failures, locally the liquid content for the formation of higher order liquid structures, such as trimers, addressed in the next section, could be reached. To avoid this artificially, and to keep the simulation in the pendular state, one can define a constant upper bridge volume V_{max}, such as $V_{max}0.057R^3$ [55]. Whenever the volume exceeds V_{max}, the excess liquid can be temporarily stored in the liquid film of the particle to be available for possible bridge formations. The second redistribution process is *liquid flux between bridges* through the wetting layers, driven by pressure differences between bridges acting on the same particle. This equilibration is rather slow and can negligible if the lifetime of a capillary bridge is much smaller than the equilibration timescale, that is usually in the order of minutes [57]. The time scale for this equilibration decreases with the inverse flow resistance $\kappa \propto \eta^{-1}$ of the film with the fluid viscosity η. For $\kappa \to \infty$ pressure between all bridges is instantaneously equilibrated, and all liquid bridges have equal Laplace pressure. For $\kappa \to 0$ bridges never, and for $\kappa > 0$ the dynamics of fluid redistribution and pressure equilibration is fully controlled by η. *Equilibration through the vapor phase* takes even longer [29] and is therefore not considered in dynamic simulations.

3.3 Extension of models for the funicular state

Starting from the pendular state, an increase in liquid content ($W_c^{max} > 0.024$) leads to merging of liquid bridges, which generates structures of increased complexity called liquid clusters, comprising more than two particles. In the funicular state one observes distinct liquid clusters of various sizes, while in the capillary state all clusters merge to form one spanning cluster. Since most clusters require three dimensional particle assemblies, they are best studied by microtomography [2, 10, 55, 67]. Scheel *et al.* [56, 57] described the richness and variety of liquid cluster morphologies in a dense packing of glass beads at various saturation degrees. Just above the pendular regime liquid bridges start to overlap, merge and form closed three particle configurations with filled pore throats, called trimers (see Fig. 7). Larger clusters emerge by merging of smaller units when the Laplace pressure reaches a critical value estimated as $-4.46\gamma/R$ [55], resulting in the formation of rather open, branched structures. Two connected trimers are called pentamers (see Fig.8(b)), three heptamers and so on (see Part 1). Four particles forming a tetrahedron with

Fig. 7 (left) Three grains with liquid bridges, (center) trimer with filled pore throat and (right) ruptured trimer with subsequent liquid redistribution.

one trimer on each face are called tetrahedral cluster (see Fig.8(a)). The pore inside can be filled or even contain a trapped gas bubble. The liquid clusters are formed when the fluid content increases, but can also decay when fluid drains from the system.

Contrary to single bridges, higher-order clusters lack rotational symmetry. Nevertheless, for trimers, numerical solutions could be found by Rynhart *et al.* [53] for equal particles for a given contact angle and constant mean curvature. Also solutions from numerical surface energy minimization like the Surface Evolver software [5] are available [62]. Such simulations give the shape of the liquid-vapor interface and the corresponding capillary forces. The analysis of Semprebon *et al.* [62] is limited to three particle configurations with a gap that varied. One observes a transition between fundamental morphological types like liquid bridge and trimer, showing slightly larger capillary forces in a trimer compared to the ones of three single bridges due to the filled pore throat (Fig. 7 a,b).

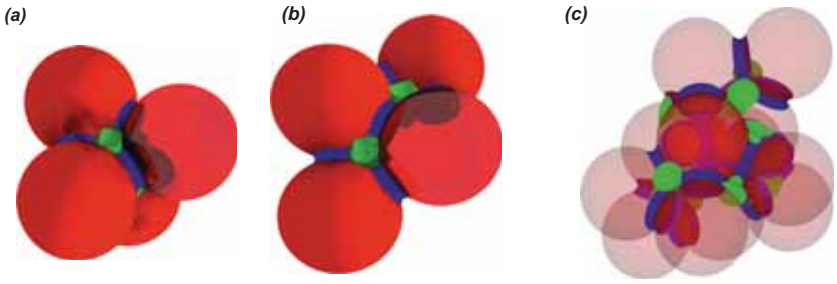

Fig. 8 (a) Tetrahedral cell (b) pentamer and (c) larger composite liquid cluster. Bridges are colored blue, menisci and pore throats green. Reprint of (a,b) by permission of APS: Ref. [42].

The distribution of liquid morphologies is highly history dependent on the particular wetting process. While mixing of grains with liquid and subsequent equilibration results in cluster morphologies observed by Scheel [57], other processes like

spontaneous imbibition can lead to completely filled regions of the packing with a single wetting front [47].

3.3.1 Geometric representation of liquid bodies

If one accepts reasonable downturns in numerical performance, the pore-space and liquid structures can be approximated rather close to their real shape. For a given granular packing, one calculates the pore-throat network via Delaunay triangulation [40]. Hence the system volume is subdivided into single tetrahedra, like the basic unit shown in Fig. 9(b). The faces of the tetrahedron form the four pore throats, while the void space in each tetrahedron is called the pore body of the cell. Pore bodies can be empty, filled, or partially filled with liquid separated by menisci. The basic strategy consists in the decomposition and representation of higher geometrical configurations such as trimers, pentamers, tetrahedral clusters, and higher ones as a combination of elementary units such as liquid bridges, menisci, or filled pore bodies. Melnikov [41] describes this approach in detail.

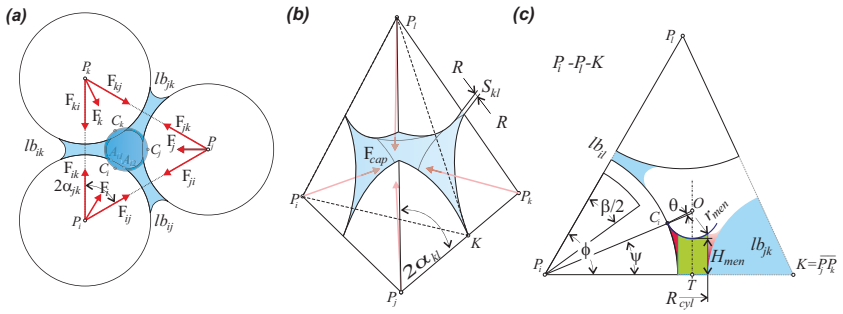

Fig. 9 (a) Trimers (b) tetrahedral cell and (c) cut through a meniscus (green) in the $P_i - P_l - K$ plane (see dashed line in (b)). Red regions highlight the volume that is not captured by the cylinder representation of menisci. Reprint by permission from Springer Nature: Ref. [43].

We start with the liquid-gas interface between three grains - the menisci - that can exhibit rather complicated shapes since we already described bridge models in Sec. 3.2. Nevertheless, we simplify them to be spherical of radius r_{men} like Haines [20], what is in satisfying agreement with experimental observations [55, 57]. A cut through a pore throat is shown in Fig. 9(c). The centers of the four possible menisci of a tetrahedral cell are located on the normal of each pore throat through the circumcenter of the respective face. With the contact angle θ and meniscus radius r_{men}, the exact position on this normal can be calculated following the method proposed in Ref. [17] (see Fig. 9(c)). Note that single menisci can only exist in combination with associated liquid bridges forming one single liquid body with its Laplace

pressure determined by the curvature of the meniscus r_{men}^{-1} via the Young-Laplace equation (Eq. 2), as $\Delta P = \gamma 2 r_{men}^{-1}$.

Similar to the bridge, a capillary force $F_{i,j,k}$ from the meniscus will act on the involved particles i, j, k in addition to the forces from the liquid bridges. It acts in the direction given by the points $P_i^{-}T$ (see Fig. 9c) with unit vector $\mathbf{e}_{iT}$ and is calculated as $F_{i,j,k} = \mathbf{e}_{iT} \cdot \Delta P A_{eff}$. The effective wetted area A_{eff} can be defined for example in a simplified fashion for particle i through the area of a triangle connecting the points $C_i A_{i1} A_{i2}$.

With the three basic units liquid bridge, meniscus, and filled pore body, in principle all liquid clusters can be composed. As an example, the smallest cluster is the trimer consisting of two menisci, located in neighboring tetrahedra on both sides of the common pore throat and their shared liquid bridges (see Figs. 7,9(a)). The volume of a cluster V_c with N_{imb} imbibed pore bodies and N_{men} menisci is given by

$$V_c(r_{men}) = \sum_{i=0}^{N_{imb}} V_{pore,i} + \sum_{j=0}^{N_{men}} V_{men,j}(r_{men}), \tag{6}$$

with the volume $V_{pore,i}$ of the imbibed pore body i and the volume $V_{men,j}$ of meniscus j including portions of the m associated liquid bridges with volumes V_i^{lb} of this meniscus:

$$V_{men,j}(r_{men}) = V_{cyl}(r_{men}) + (0.5 + \varepsilon) \sum_{i=0}^{m} V_i^{lb}(r_{men}). \tag{7}$$

One approximates the fluid volume of the pore throat V_{cyl} by a cylindrical body volume coaxial to the normal of the pore throat (Fig. 9(c)) with radius $P_i^{-}T - R_i$ and its upper surface delimited by the meniscus. Note that the cylinder height H_{cyl} can be negative if in the neighboring tetrahedral cell the pore body is filled. In this case, the volume of the neighboring pore body needs to be reduced by the volume given by the intersection of the meniscus with the throat pore plane. The cylinder-sphere cap approximation systematically underestimates real volumes, what can be taken care of via a geometrical correction parameter ε in Eq. 7 that will be determined later on from experiments. Index m is between 0 and 3, depending on the number of connected liquid bridges. If a meniscus shares a liquid bridge with an adjacent meniscus, as for a pentamer in Fig. 8(b), m for one of the menisci is reduced by 1 to avoid double counting of bridge volumes. Note that for every meniscus only half of each liquid bridge volume is considered since the other half is located in the opposed triangulation cell if its pore body is not saturated. For tetrahedral cells with filled pore body, the Laplace pressure pulls each of the four particles towards the center as shown in Fig. 9 (b). One represents the respective wetted area by the one of the liquid bridge with opening angle β_{ij} for cases with a liquid bridge between the corresponding particles. For simplicity, the force direction is not corrected and keeps pointing towards the cell center. For entirely immersed particles, forces from the pore body cancel each other out. Tetrahedral cells with four menisci may comprise an incompressible, trapped gas bubble.

To summarize, in a cluster, liquid bridges are always associated with one of its menisci creating a common liquid body with equal pressure defined by the meniscus radius r_{men}. One calculates the maximum liquid volume of the filled pore via the difference of the tetrahedral cell volume and the partial volumes of the four particles contained within the cell.

3.3.2 Evolution laws of liquid bodies

Liquid clusters evolve when their volume changes due to sources, sinks, condensation, evaporation, or merging with other clusters as well as relative movements of involved grains. Stability criteria for drainage and imbibition with instantaneous jumps between stable configurations control the evolution of liquid clusters. These interface jumps are micro-mechanically associated with drainage or imbibition of pore bodies or throats or bridge rupture. A limited set of geometrical instability criteria for imbibition (***i1-i4***) and drainage (***d1-d3***) can be identified, similar to Refs. [17, 48], itemized below:

i1 When two liquid bridges with filling angles $\beta_{ij;ik}$ touch each other, they can form a new trimer by filling the pore throat, provided that sufficient liquid for a stable meniscus (drainage criterion ***d1***) is available. With the opening angle α_{jk} (see Fig.9(a,b)) it reads $0.5(\beta_{ij}+\beta_{ik}) > 2\alpha_{jk}$.

i2 If a meniscus in a tetrahedral cell touches a single liquid bridge that is presently not part of the liquid body, the pore body is filled (Melrose criterion [44]). Hence, the respective meniscus with the filling angle of the meniscus ψ and the face-edge angle ϕ shown in Fig. 9(c) becomes unstable when $\psi + \beta/2 > \phi$.

i3 When centers of two menisci inside one pore body touch each other, they build a single spherical interface and can fill the pore body. However, in the case when all four menisci already exist, a gas bubble gets trapped.

i4 When a meniscus touches the opposite particle, the pore body is imbibed.

d1 When pore throats are reduced to a minimum size, given by the critical height of the menisci $H_{min}^{men} \geq \lambda R$ with the drainage parameter λ, they drain. Best agreement with experimental data is found for $\lambda \approx 0.15$ [42] (see Fig. 13).

d2 When the center of the meniscus of a neighboring cell touches the respective pore throat plane of an entirely saturated cell, the pore body becomes unstable. Instantaneously the liquid interface jumps to a new stable position, and the pore body is drained.

d3 Liquid bridge failure as described by Eq. 5.

Inside one liquid body instantaneously pressure equilibration and respective fluid flow are assumed. Transport in between spatially disconnected liquid clusters that share at least one grain, however, is assumed to occur via a liquid film on the particle surface, inspired by experimental observations by Refs. [34, 55]. The volume flux $\dot{V}_i$ into structure i is proportional to the local Laplace pressure differences of the involved liquid clusters. If N_i clusters connect to the same grain,

$$\dot{V}_i = \frac{R}{\gamma} \cdot \sum_{j=0}^{N_i} \omega_{ij}(P_j - P_i) \tag{8}$$

with the dimensionless conductance coefficient ω_{ij}, determining the equilibration timescale. ω_{ij} comprises details such as the distance between clusters or the number of clusters connected to the grain and others [35, 38]. However, for simplicity, typically a constant value for $\omega_{ij} = 0.01$ is chosen. With all the described model building blocks at hand, we can now turn to simulations.

3.4 Pressure-controlled simulation variant

To this point, the liquid transport within the saturated region of the pore space was assumed to occur instantaneously. This hypothesis is a valid assumption for small liquid clusters. However, if larger filled regions of the pore space are concerned, the flow is limited by the permeability of the granular material and the viscosity of the fluid. For modeling of large liquid clusters connected to a reservoir, pressure-controlled models like classical imbibition models are a better choice. This can also be motivated by the calculation of Haines jumps in Sec. 4.2 Fig. 16, where the pressure dependence on single imbibition events in the form of pressure jumps rapidly decreases with increasing cluster volume. Using the representation of the liquid-gas interface described above, it is also possible to introduce a pressure-controlled imbibition model which can simulate the unsteady liquid infiltration into the unsaturated granular material.

The pressure controlled simulation model is based on the assumption that pressure inside each pore is constant and pressure drops occur at pore throats (see Fig. 9(b)). The liquid flux q_{ij} occurs between neighbor cells i and j due to the local pressure gradient ΔP_{ij}. If all four neighbors $j = 0, ...4$ of a given saturated pore i are also completely filled with liquid, the continuity equation for this pore reads

$$\sum_{j=0}^{4} q_{ij} = 0, \tag{9}$$

meaning that the overall liquid volume in this pore is conserved. However, if one or more of the neighbor pores are empty like for all pores at the liquid front, the total flux into or out of the given cell i is not necessarily zero, hence

$$\sum_{j=0}^{4} q_{ij} = Q_{eff}. \tag{10}$$

Here, the net in- or outflow from the cell i is denoted as Q_{eff}. This volume change results in changes of the bounding menisci of this cell due to volume conservation since at least one neighbor cell is not saturated. The volume Q_{eff} is used to find the new pressure in the cell i and to recalculate its menisci. Due to in- or outflow the

menisci can become unstable (criteria **i1-i4**, **d1-d3**) which results in imbibition of neighbor pores or in drainage.

The liquid flux occurs through pore throats which have different geometrical shapes and q_{ij} can be calculated based on the geometrical properties of the pore throats. Both, the Stokes and the Darcy equations assume a linear relationship between the pressure gradient and the flux is

$$q_{ij} = g_{ij}(p_i - p_j), \tag{11}$$

with g_{ij} being the local conductance coefficient between two pores with respective pressures p_i and p_j. g_{ij} takes into account the geometry of the pore throat calculated via an approach originally introduced by Bryant *et al.* [7]. In this approximation the flow through the pore throat is assumed to be a Hagen-Poisueille flow through a cylinder of radius r and length l_{ij}:

$$g_{ij} = \frac{\pi r^4}{8\eta l_{ij}}, \tag{12}$$

where η denotes the viscosity of the fluid. Since the pore throat does not have a circular shape (see Fig. 9(c)), an approximation can be used for the radius $r = r_{eff}$. One of the possible definitions of the effective radius of the pore throat r_{eff} is given in Ref. [7] via $r_{eff} = 0.5 \cdot (r_c + r_e)$ where r_c denotes the radius of the inscribed circle inside the pore throat and r_e the radius of the circle with the same surface as the pore throat. One defines the effective flow path length l_{ij} as the distance between the centers of the cells i and j. The center of the cell is the point which is equidistant from the centers of all four particles. One uses the projection of this point onto the nearest cell face if this point lies outside of the cell body.

To run simulations, first the pore-throat network must be extracted, and entry pores with respective pressure must be defined. Then the instability criteria **i2** – **i4** are checked, resulting in pore imbibition. When one fills a new pore, one sets its pressure to the minimal possible value which allows the formation of stable menisci. The new pressure creates suction on the liquid phase, supporting the flow towards the liquid front. In the next step a system of linear equations based on Eqs. 9 and 10 is formulated and solved e.g. with the LAPACK sparse matrix solver provided in the *Armadillo* library [54]. The calculated flows are used to update the pressure in completely saturated pores. One uses the volume conservation constraint to update the pressure in the saturated boundary pores next to the liquid front.

4 Simulations for wet particle assemblies

To construct the initial mono-disperse particle packing, a random sequential adsorption [13] of equally sized spheres inside the sample volume V_{sample} with periodic boundary conditions (PBC) is employed. One adjusts the solid fraction Φ_s by increasing particle radii R while particles can rearrange. An initial liquid vol-

ume is given to each particle, to keep the system in the pendular regime where only liquid bridges exist. The liquid content W_c is defined by the total volume of the liquid V_{liquid} normalized by the void volume V_{void} as $W_c = V_{liquid}/V_{void}$. V_{void} is calculated as the difference between V_{sample} and the total volume of all N_p grains R: $V_{grains} = 4\pi N_p R^3/3$. Consequently the porosity can be calculated with $\Phi = 1 - V_{grains}/V_{sample}$. We simulate different features of fluid transport and configurations in wet granular assemblies in the pendular (Sec. 4.1) and funicular state (Sec. 4.2), as well as consequences on the rheological behavior (Sec. 4.4).

4.1 Fluid motion in sheared unsaturated granular media

With the particle packing and initial homogeneous liquid content of $W_c = 1\%$ we simulate shear flow in the circular split bottom shear cell described in Sec. 2.2. One uses periodic boundary conditions for a small segment with arc length 0.0873 and hydrophobic cell walls. One considers gravity and calculates capillary forces via Eq. 4. Whenever particles contact, a liquid bridge is formed, while particle separation beyond s_c results in bridge rupture (criterion ***d3***) [23, 65]. One determines the fluid redistribution by the combined pressure-distance relation (Sec. 3.2). The inverse flow resistance of the film κ (Sec. 3.2) controls the pressure equilibration.

When comparing the outcome of simulations in the steady state, reached after eight rotations, to the experimental data (Sec. 2.2) we see that for $\kappa = \infty$ (instantaneous pressure equilibration), the liquid content W_c is proportional to the number of contacts, but not to the measured liquid content (see Fig. 10(b)). For $\kappa = 0$, however, the steady-state liquid distribution shows good agreement with experiments and a clear depletion from the shear zone (Fig. 10(a)). Hence, in this system with glue as a liquid, equilibration times of liquid bridges are much larger than contact times of the beads in the shear band. Consequently, liquid redistribution is mainly taking place via bridge rupture events, leading to liquid fluxes away from the shear zone. One can generally conclude that in shear bands of wet particle packings, not only the coordination number but also the average bridge volume is reduced [37].

In general, granular systems under shear can form quite different shear profiles, depending on the hydrostatic stress. High stresses exhibit alternating diffuse and localized shear that result after averaging in a rather linear shear velocity profile. For low confining pressure P (see Fig. 11(a)) capillary forces play an important role and stresses from the shear deformation are less capable of rupturing bridges. Consequently, the velocity profile depends on the fluid distribution, since wet grains stick together. In Mani *et al.* [36] the effect of the stress state on the transport behavior was studied by using a cohesion number $\eta^{coh} = F_c^{max}/PR^2$ giving the ratio of the largest cohesive force to the one exerted on a particle. For this purpose the particle packing was loaded with a plate at a variable pressure P and using periodic boundaries (in x, y directions) again, the system was sheared as depicted in Fig. 11(a). Initially, liquid is only placed in bridges close to the center with a Gaussian distri-

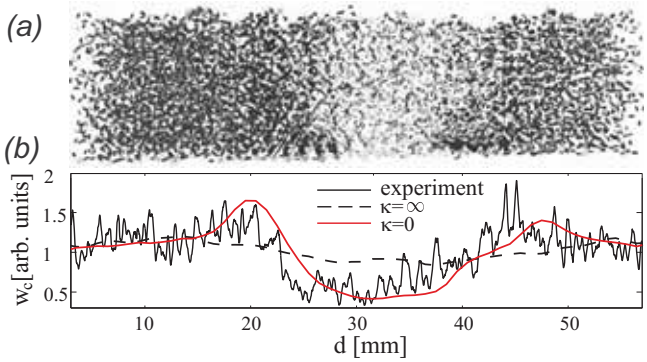

Fig. 10 (a) A slice perpendicular to the the shear band showing capillary bridges as lines of width and darkness proportional to their volume. (b) Liquid content as function of radial position after 8 rotations compared to the experiments (Sec. 2.2) for different values of κ. Reprint by permission of APS: Ref. [37].

bution for the bridge volume $V_b(z) = A\exp(-(z - z_{wall}/2)^2/\sigma_0^2)$ with amplitude A and width σ_0.

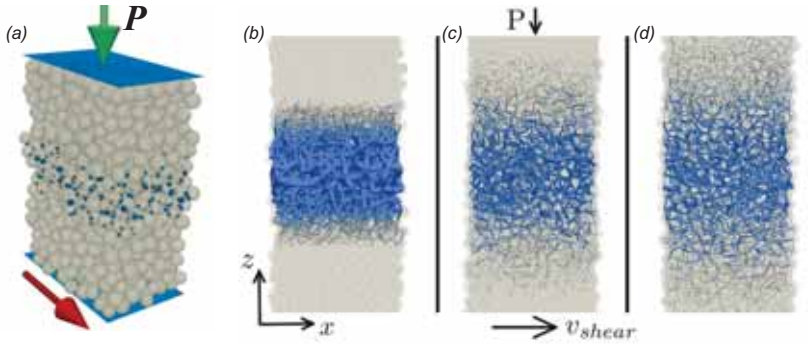

Fig. 11 (a) Plane shear cell with periodic boundaries and fluid initially located in the center. (b-d) Snapshots of the liquid configurations in a slice, located in the central part under shear at the beginning (b), at an intermediate stage (c) and at the end of the simulation (d). The bridge volume V_b is indicated by the width of the lines, connecting the sphere centers. Reprint (b-c) by permission of Springer Nature: Ref.[36].

In the snapshots of Fig. 11(b-d) one can easily see that the liquid is spreading toward the top and the bottom wall during the simulation. Quantitatively this is shown by the average bridge volume per particle Q in Fig. 12 for various cohesion numbers η^{coh} and at different deformations γ. For high confining pressure P

($\eta^{coh} = 0$) a nearly linear shear rate profile is measured, while for high η^{coh} particles in the wet zone adhere, forming a plateau in the shear rate profile that is more pronounced as η^{coh} increases and finally controls liquid distribution (Fig. 12). Due to the linear shear profile, the initially Gaussian liquid content profile is kept, pointing at diffusive transport [63]. The diffusion constant D is found to be a function of the initial moisture amplitude A of the type $D(A) = a/(1 + bA^{1/3})$ with $a = 0.633R^2$; $b = 2.936R^{-1}$. Qualitatively the decreasing diffusivity for increasing liquid content can be explained by larger rupture distances s_c of bridges and thus decreased rupture rates, since this is a main liquid redistribution mechanism, next to the diffusive motion of particles under shear [8, 66]. Diffusion of particles

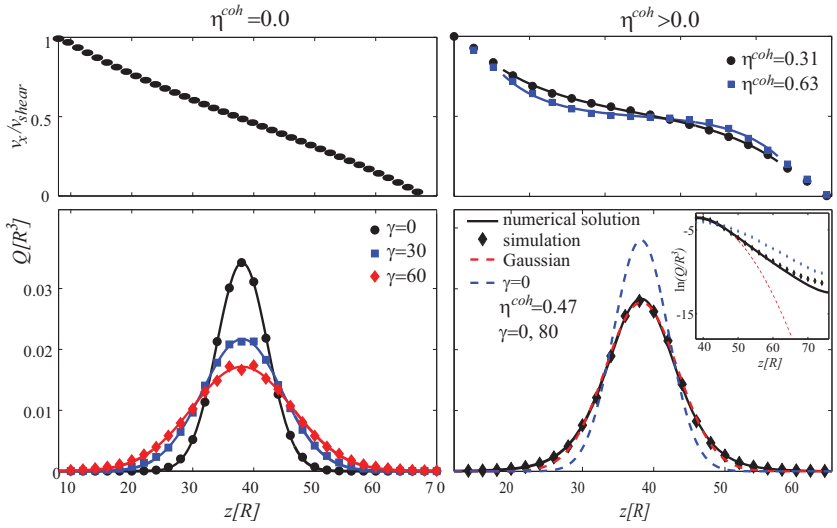

Fig. 12 Shear velocity profiles (top row) and average liquid contents as a function of the height z (bottom row) for large (left column) and low (right column) hydrostatic stresses. The inset (bottom right) highlights the deviation from the Gaussian distribution. Reprint by permission of Springer Nature: Ref.[36].

and liquid bridge ruptures are also important processes for higher cohesion numbers. However, both depend on the reduced shear rate in the wet region. We observe the largest deviation from the diffusive Gaussian at the borders between the wet and dry region ($z \approx 50$) from the liquid profiles (Fig. 12). In practice, this results in the known difficulty of mixing dry and wet powder. On can improve the mixing process by decreasing η^{coh}, in other terms increasing the hydrostatic stress, since local shear rates determine the liquid migration [36].

4.2 Granular assemblies at arbitrary saturation

The previously shown simulations (Section 4.1) only consider the interaction between single particles with no need for the consideration of the pore space. In a first study, after the construction of the packing, all particles are immobilized for the remainder of the simulation to first focus on the evolution of liquid clusters as liquid is injected (removed) at a specific position or condensed (evaporated) at gas-liquid interfaces. The system is subdivided into tetrahedral cells by a Delaunay triangulation of particle centers, and liquid bridges are allowed to equilibrate pressure. Note that the Delaunay triangulation is the dual graph to a Voronoi diagram used in a comparable context in Ref. [71]. In this simulation, liquid volume is the control variable. Consequently, volume changes, e.g., due to condensation into already existing bridges, result in an update of all liquid structures to make the Laplace pressure correspond to the changed volume. Changes in the liquid cluster morphology can trigger instabilities. We check the instability criteria (Sec. 3.3.2) for imbibition ***i1-i4*** and drainage ***d1-d3*** in ascending order, because first menisci must form before pore bodies can be filled. The entire cluster needs to be updated when one adds a trimer to a cluster due to criterion ***i1***. The same holds when one merges a cluster with a trimer. One eliminates identified instabilities through drainage or imbibition and performs a cluster update. Resulting pressure differences again drive liquid transport through liquid films (Eq. 8) that changes liquid clusters and so forth. One repeats this procedure until convergence before adding or removing any additional fluid. To ensure liquid volume conservation, one subsequently recalculates all liquid clusters. To speed up simulations, we interpolate from tabulated values for the liquid bridges [38]. Those originate from simulations with the numerical energy minimization method (NEM) of the software SURFACE EVOLVER as discussed in Part 1[5]. Note that the contact angle θ is kept constant at 5° in the following.

Calibration with trimer formation and decay: First we calibrate the model on experimental data from Ref. [57] by simulating three particles that form trimers when liquid is condensed at liquid-gas interfaces (criterion ***i1***) and decay, when liquid evaporates or opening angles change (criterion ***d1***). The liquid bridge pressure P is updated to correspond to the changing volume. During condensation, the bridges coalesce, and a new trimer is created at the critical dimensionless value P_{max}. Consequently, P drops, since the liquid needed to fill the pore throat which previously was part of the bridges that decreases the radius of the interface curvature. During evaporation, the trimer decays into three liquid bridges at the critical minimal dimensionless pressure P_{min}. Good agreement with experimental data is obtained with the geometrical correction factor $\varepsilon = 0.07$ (see Eq. 7) and the drainage parameter $\kappa = 0.15$ for the drainage criterion ***d1*** as shown in Fig. 13(a). The critical minimal pressure P_{min} of a trimer strongly changes with the inter particle separation distance s_{ij} or the corresponding opening angles α_{ij} (definition see Fig. 9). When $s_{ij} \leq s_c$ (criterion ***d3***) a bridge and consequently the trimer can no longer exist. Fig. 13 (b) shows the pressure curves for a trimer when one of the opening angles α_{ij} is increased while the other two contacts remain closed. High P_{min} are associated with large values of α_{ij}. For imbibition this implies that trimers with non-contacting par-

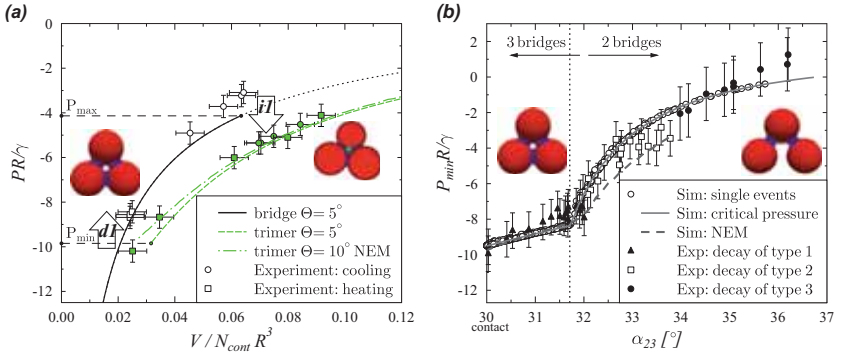

Fig. 13 (a) Comparison of the dimensionless Laplace pressure of a trimer and liquid bridges between three contacting particles as a function of their volumes V normalized by the number of contacts $N_{cont} = 3$ and the grain radius R^3. Trimers form at P_{max} and decay at P_{min} (for $\theta = 5°$). (b) Trimer decay: Dependence of P_{min} on the opening angle α_{23} for trimers. Three types of trimer decay are possible: (1) decay into two liquid bridges, (2) slow transition into two liquid bridges, and (3) decay into three liquid bridges. Only configurations with one gap opposite to the opening angle are presented. Experimental data and NEM results by Ref. [57]. Reprint by permission of APS: Ref. [42].

ticles form at higher overall Laplace pressures compared to contacting ones. To prove the validity of this assumption, we compare the resulting dependence of P_{min} on α_{ij} with measurements (see Fig. 13(b)) from evaporation experiments. Our predictions are correct within experimental error bars and we observe two different regimes separated by an angle $\alpha_{ij} \approx 31.7°$. Below, the drainage criterion ***d1*** is fulfilled, while above bridge rupture (***d3***) occurs. Interestingly, the NEM results from Ref. [57] agree less with the experimental data than our simplified approach.

Liquid clusters in larger particle assemblies: In unsaturated granular packings, a multitude of different cluster morphologies and sizes coexist. Scheel evaluated them in his thesis for a random, monodisperse packing of spherical particles with solid fraction $\Phi = 0.57 \pm 0.01$ at liquid contents in the range $0 < W_c < 0.2$ [57]. We simulate this case by incrementally condensing liquid into a particle packing consisting of 2000 particles with periodic boundary conditions in all three directions via the procedure described above. Fig. 14 shows a snapshot of the liquid clusters present at the beginning of the funicular regime at $W_c = 0.03$. The distribution of morphologies shows a fast transition between the liquid regimes (see Fig. 15). At low W_c only bridges exist, while the regime above the pendular state shows a rapid increase in the number of clusters. It reaches a maximum when the merging into larger clusters starts to dominate. Finally, only a single spanning cluster remains. The simulations reproduce the general trends observed in the experiments. However, deviations due to finite sample sizes and experimental resolution are visible. A similar picture is found for the proportion of liquid stored in different morphologies as a function of W_c (see Fig. 15(b)) where one can see that at $W_c = 0.2$ more than 95% of the liquid volume is located in large clusters.

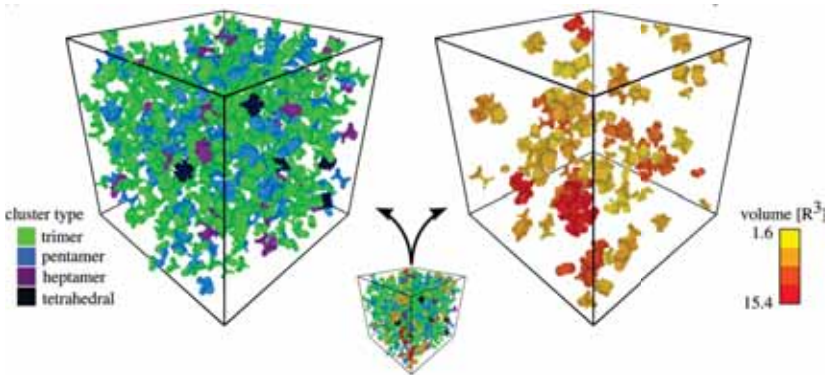

Fig. 14 Rendering of liquid clusters without bridges (center) at $W_c = 0.03$ split up into tow images for small (left) and large (right) clusters for clarity. Reprint by permission of APS: Ref. [42].

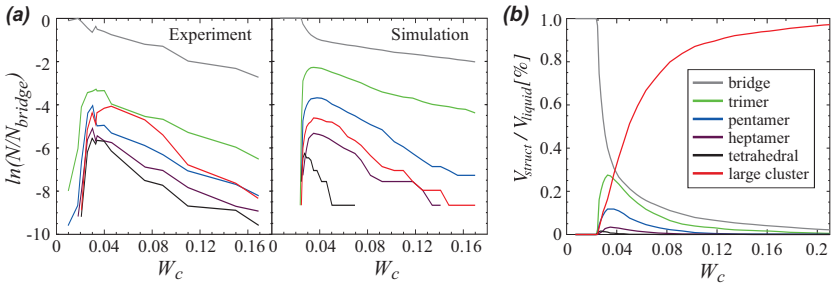

Fig. 15 (a) Comparison between simulation and the experiments of Ref. [57] of the number of different liquid cluster morphologies N scaled by the total number of existing liquid bridges N_{bridge} (at $W_c \approx 0.02$) for $\Phi_s = 0.57$ as function of the liquid content W_c. (b) Proportion of liquid V_{struct}/V_{liquid} stored in different morphologies as a function of W_c. V_{struct} is the summed volume of all morphologies. Liquid structures larger than heptamers are called large clusters. Reprint by permission of APS: Ref. [42].

Evolution of single liquid clusters: When clusters grow or contract, pressure jumps originating from rapid imbibition of single pore bodies or their drainage are observed. These so-called Haines jumps have been observed experimentally by Berg *et al.* [2] and are due to volume conservation for the new configuration, resulting in increasing or decreasing curvature of menisci. As local instabilities drive the liquid interface propagation, we model it as a discontinuous process jumping from one stable configuration to the next one. We show the evolution of the pressure in one liquid body that forms by injecting liquid with a constant flux at a single point (Fig. 16). First, the dimensional cluster pressure increases, until due to trimer formation a sharp drop occurs. Each drop is due to a local instability of filling a new pore body or a throat. The decreasing magnitudes of jumps with cluster size are due

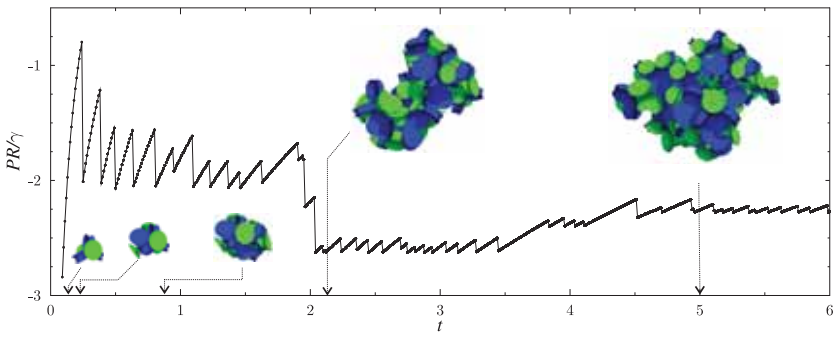

Fig. 16 Evolution of dimensionless Laplace pressure of a liquid cluster for liquid injection at a constant flow rate at one source point. Reprint by permission of APS: Ref. [42].

to the relation of the liquid volume needed for the filling of the next pore to the total cluster volume. With the conductance coefficient $\omega = 0.01$, the flux can be fast compared to the liquid transport through surface films. Jumps from small clusters can be compared to experimental data [55], while for larger clusters no data is available.

4.3 Pressure controlled imbibition front formation

In this simulation a discontinuous propagation of the liquid interface is studied in a dense packing with $N_p = 1750$ particles [41]. Unlike the simulations described up to now, the process is controlled by fluid that enters the system under a given pressure (compare Sec. 3.4). We fill the entry cells in the upper boundary of an initially dry sample with liquid and set the pressure to a constant value of $PR/\gamma = -3$. Additionally, we consider the effect of gravity (hydrostatic pressure) by introducing a pressure gradient in the z-direction. The pressure on the upper boundary is maintained constant during the whole simulation. This boundary layer is thus assumed to be directly connected to a reservoir. Due to instabilities, we fill new pores as the interface propagates through the material. The filling of a new pore is only possible if enough liquid is available in the neighbor pores. Due to the filling of a new pore, the pressure of the liquid phase inside the pore is lower than in the neighboring pores since only a limited amount of liquid is available. Note, that in this model the sample has a finite permeability since fluid transport in now not instantaneous but exhibits viscous flow. Therefore, liquid first needs to be transported from the reservoir to the newly filled pores. After the filling of a new pore, a subsequent inflow through the neighbor pore throats leads to an increase in capillary pressure during the next time steps until reaching a steady state or a new instability. The filling of new pores creates a pressure gradient in the sample which leads to suction of liquid from the reservoir. Fig. 17 shows snapshots of the liquid body at different time steps

during the simulation, colored according to the pressure field. Fig. 17(a) shows the filled entry pores at the initial time step ($PR/\gamma = -3$). During the next time steps, due to instabilities, new pores are filled Fig. 17(b)-(c). One can see, that the pressure field varies throughout the liquid body. The pressure remains constant in the entry cells (upper layer). The newly filled cells at the interface have a significantly lower pressure of approx. $PR/\gamma = -10$. Finally, there are also cells with a higher pressure than in the entry cells due to gravity.

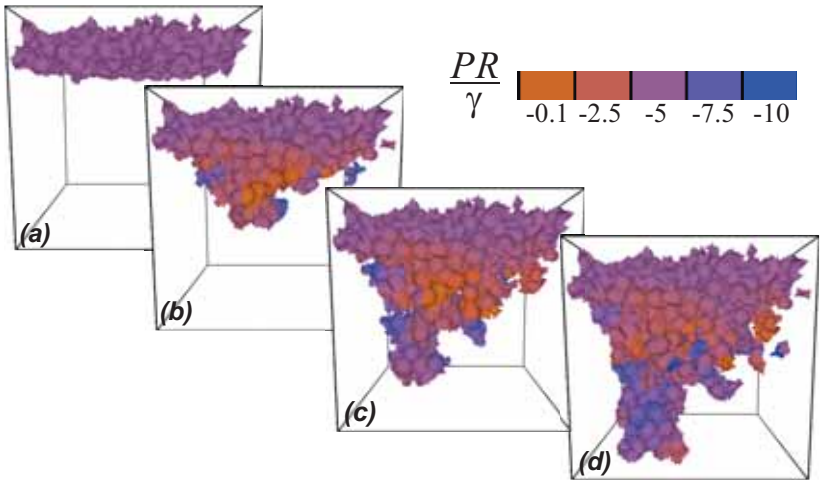

Fig. 17 Time evolution of an imbibition front in a sample with $N_p = 1750$ particles (not shown). The pressure in the upper particle layer is kept constant at $PR/\gamma = -3$. We show only the liquid phase consisting of filled pore bodies. Note that we use periodic boundary conditions in horizontal directions. (a) Initial front; (b) Front with finger formation and (c) front shortly after (b). (d) percolating cluster.

4.4 Fluid induced failure

In a rigid porous body from sintered glass beads, one can omit the coupling between fluid and particles. In frictional granular systems, however, even at high hydrostatic stress states, a significant number of so-called spectator particles does not directly contribute to the contact force network. The coupling between fluid and particles changes particle configurations and liquid clusters add macroscopic cohesion via the Laplace pressure to the system. The fluid couples to the particles via the forces described for liquid bridges in Eq. 4 and pore throats and bodies in Secs. 3.3.1. Due to the complexity of higher order liquid bodies, described above, simulations

are predominantly limited to the pendular state (e.g. [18, 35, 36, 51, 59, 60]). With simplified geometrical assumptions, described in Sec. 3.3, however, this limitation can be overcome. In soil mechanics, the effect of the internal pressure field on the macroscopic behavior is of wide importance not just for sand sculptures, but for slope stability in general. Triaxial shear tests on cubic samples are simulated at different initial saturation states to capture the effect of hydrostatic stress on such systems [1, 43]. The cubic sample contains 5000 particles of mass density $\rho_p = 1$, radius $R = 1$ and resulting mass m_p. First, we assign random velocities to all particles. After randomization, the sample is confined by hydrostatic pressure on the box walls with suppressed contact friction $\mu = 0$ until a solid fraction of $\Phi_s = 0.6$ is reached at a cube edge length L of about $32R$ (see Fig. 18). Triaxial tests require

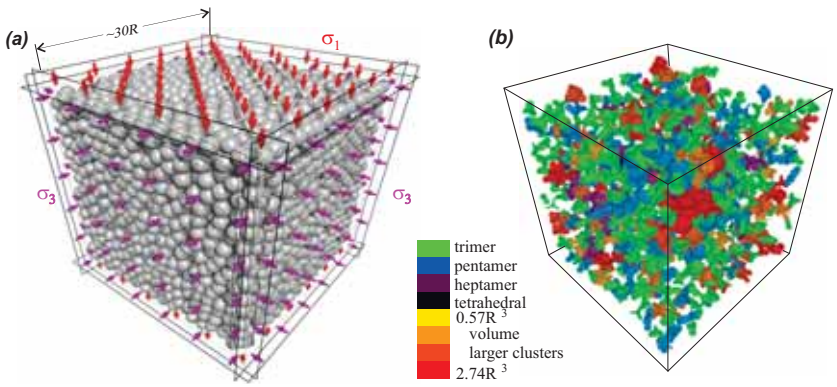

Fig. 18 (a) Setup of the triaxial shear test with confining walls and (b) liquid clusters emerging at liquid content $W_c = 3\%$ with colors representing cluster morphology and size. Reprint by permission from Springer Nature: Ref. [43].

confining forces on each wall F_{conf}, that are calculated with the respective stress $\sigma_{1,2}$ and the true area of the wall A_{wall} involved. For the compression, μ is set to 0.3 and the surface tension $\gamma = 1$. The hydrostatic stress σ_3 is applied on all movable side walls, the bottom wall is fixed and the upper wall lowered at a constant strain rate $\dot{v} = v_w/L_z$ with the vertical displacement rate v_w that stays within the quasi-static limit. The differential stress is defined as $q = \sigma_1 - \sigma_3$ and axial ε_a, as well as volumetric strain $\varepsilon_V = \Delta V/V_0$ are calculated from the present and initial wall positions. The macroscopic behavior of the system was simulated with increasing initial liquid content W_c up to 40% and confining pressure $\sigma_3 = 20, 40, 60$ in units $u_p = m_p/(T^2 R)$ where T is the unit of time defined as $T = 1/\dot{v}$. To allow for a direct relation between the contact dynamical simulations with physical data, the ratio of inertial to confining forces can be used as proposed in Ref. [52]: $I = \dot{v}R\sqrt{\rho_p \sigma_3}$. Consequently for the three confining stresses this ratio is equal to $I_{20} \approx 2.2 \cdot 10^{-5}$, $I_{40} \approx 1.6 \cdot 10^{-5}$, $I_{60} \approx 1.3 \cdot 10^{-5}$.

Granular systems are typically dilating under load. The dependence on the confining pressure σ_3 is shown in Fig. 19(a) with the typical decrease in volumetric strain ε_V for increasing σ_3 similar to Ref. [59]. When comparing wet to dry cases, slightly higher values of ε_V are observed for $W_c = 1\%$ (see Fig. 19(a)). This observation could be due to attractive capillary forces that hinder spatial rearrangements. During the compression, $q = \sigma_1 - \sigma_3 [u_p]$ is calculated as function of the axial strain ε_A. q rapidly increases for small ε_A, almost independently on the liquid content W_c what is in agreement with comparable experimental [68] and numerical observations [1, 59]. In the course of the compression, q reaches a constant, moisture dependent plateau. Note that the volume exclusion constraint of contact dynamics leads to a slightly exaggerated increase in q at the beginning of the loading, contrary to soft particle dynamics, where particles are allowed to overlap (see, e.g., Ref. [60]). Clearly one can observe an increase for the maximum differential stress q_{max} or

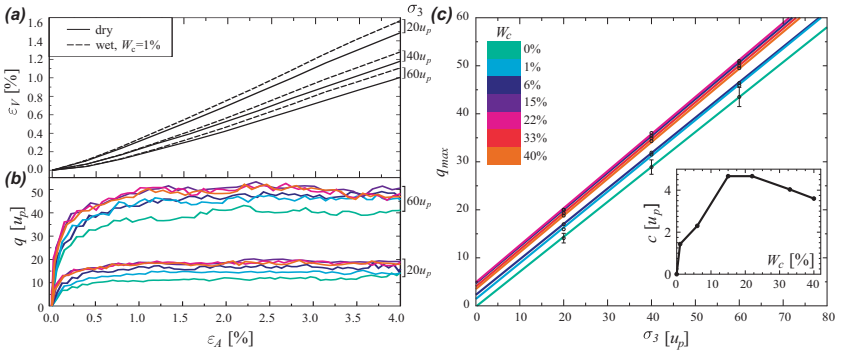

Fig. 19 (a) Volumetric strain ε_V and (b) differential stress q as a function of axial strain ε_A for different confining pressures σ_3. Liquid contents W_c have identical legend as (c). (c) Mohr-Coulomb failure envelope with maximal values of differential stress q_{max} as a function of confining pressure σ_3. Inset: Dependence of cohesion c on W_c. Reprint by permission from Springer Nature: Ref. [43].

shear strength for wet samples for identical σ_3 (see Figs. 19(b,c)). Shear strength τ versus confining pressure σ_3 can be approximated by a straight line passing through the origin for dry granulates as proposed by the Mohr-Coulomb failure criterion in the form $\tau = \mu_f \sigma + c$, where $\mu_f = \tan(\theta)$ is called internal friction coefficient, θ angle of internal friction and c cohesion. As seen in Fig. 19, similar behavior is found for wet cases ($W_c > 0$), only with $c > 0$ resulting from the sum of capillary forces of all liquid bridges and clusters. For the entirely dry and fully saturated state $c = 0$, a maximum in cohesion must exist, that is located in the funicular state in the interval $15\% \leq W_c \leq 22\%$, with a maximal increase in τ of about $5u_p$, independent on the confining pressure (see Fig. 19(c)inset). θ proves to be independent on W_c within our statistical error bars at $\theta \approx 35.9^\circ$.

Since we resolve liquid structures, their evolution during compression is accessible. Exemplary the evolution of morphologies at one distinct liquid content $W_c = 6\%$

with confining pressure $\sigma_3 = 60u_p$ is shown in Fig. 20 (a). The values are related to the initial state to highlight the relative change during axial compression. As the system dilates, inter-particle distances increase and consequently single bridges rupture, and their liquid fuels the formation of new higher order clusters. Hence, mechanical deformation triggers multiple instabilities leading to trimer formation and consolidation of existing clusters into larger structures by coalescence. This evolution is exemplified by looking at a single compact liquid cluster, previously formed by liquid injection at a single position of an initial volume $V_0 \approx 100R^3$. As shown in

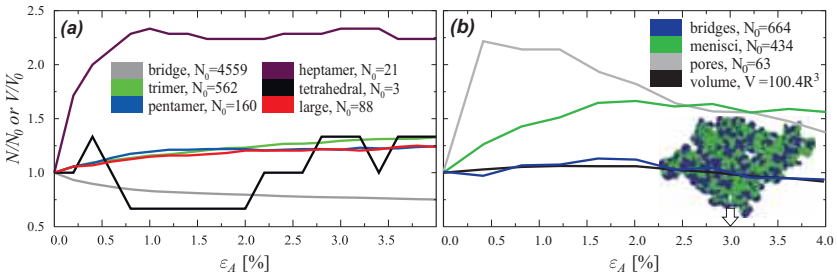

Fig. 20 (a) Evolution of liquid cluster morphologies relative to the initial configuration as function of ε_A for $W_c = 6\%$ and $\sigma_3 = 40u_p$. (b) Same as (a) but for the elemental parts of one large cluster. Reprint by permission from Springer Nature: Ref. [43].

Fig. 20(b), the cluster volume is rather constant during compression, but significant changes occur in the number of individual units which constitute the cluster. One observes a spreading and loosening of the cluster orthogonal to the axial loading direction. The increasing number of menisci is due to the formation of new trimers or the merging of trimers with already existing ones in the cluster. Interestingly, the number of filled pore bodies and liquid bridges decreases after reaching a local maximum, what is due to dilatation and thus increasing inter-particle distances. Note that the initial strong increase of menisci and filled pore bodies do not result in a higher cluster volume since Laplace pressure decreases when new pores are filled, resulting in a decrease of other menisci volumes as they move deeper into pore throats.

5 Conclusions and Outlook

With the fluid-particle models described in this chapter, one can study the shearing behavior of granular packings under different saturation levels, ranging from the dry material via the capillary bridge regime to higher saturation levels with percolating clusters, even up to the fully saturated state. The complexity of liquid morphologies is taken into account, implying the formation of isolated arbitrary-sized liquid

or gas clusters with proper Laplace pressures. The core of our novel fluid-particle model is the discretization of the complex liquid morphologies by three basic liquid structures: bridges, trimers, and tetrahedral cells. Those are combined to form arbitrary-sized liquid clusters with proper Laplace pressures that evolve by fluid exchange via films on the grain surface. Depending on local conditions, changes of accessible liquid and the pore space morphogenesis, determined by the granular phase, liquid clusters can grow in size, shrink, merge and split. We represent the coupled solid phase by a discrete particle model based on Contact Dynamics, where capillary forces exerted from a liquid phase add to the motion of spherical particles. With the model, we study the failure of systems at various liquid contents under multi-axial stress states, the change in fluid distribution and morphologies during the loading due to the deformation of the pore space, drainage, and imbibition, as well as imbibition front instabilities like viscous fingering, using a pressure-driven model.

The usage of the models is demonstrated in studies on the fluid transport in sheared granular media, exhibiting the critical role of confining pressure on the diffusion mechanism. We show a study on the role of contact angle hysteresis in Part 1 of this work. Exact calculations of the liquid surface morphologies of the liquid bodies are impracticable for larger grain assemblies. However, we demonstrated how to use findings from NEM simulation (Part 1) in grain scale simulations with a large number of particles. It is likely that in the future, one extends the parameter space for NEM simulations concerning contact angles, surface tension, and variable particle radii, what would immediately allow for extensions of the described DEM models, e.g., to capture contact angle hysteresis, poly-disperse packings, and non-hydrophobic boundaries. In the current version of the model also a limitation to small strains up to $4-5\%$ is inherent since we did not include updates and mappings of triangulation structures. For higher strains, the particle positions must be triangulated anew to provide a valid pore network. Another extension of the model could be the consideration of liquid transport through the gaseous phase to consider liquid with low vapor pressure or a low-pressure environment, as well as hydrostatic pressure, essential to understanding viscous fingering.

Acknowledgements We would like to thank Ciro Semprebon and Martin Brinkmann for providing tabulated values characterizing single liquid bridges, M. Rüggeberg for support in making Figs. 6-7, and the Deutsche Forschungsgemeinschaft (DFG) for financial support through grant no. HE 2732/11-1. The research leading to these results has also received partial funding from the People Programme (Marie Curie Actions) of the European Unions Seventh Framework Programme FP7 under the MUMOLADE ITN project (Multiscale Modelling of Landslides and Debris Flow) with REA Grant Agreement No. 289911, as well as from the European Research Council Advanced Grant No. 319968-FlowCCS.

References

[1] Belheine, N., Plassiard, J.P., Donz, F.V., Darve, F., Seridi, A.: Numerical simulation of drained triaxial test using 3D discrete element modeling. Computers and Geotechnics **36**(1), 320–331 (2009)

[2] Berg, S., Ott, H., Klapp, S.A., Schwing, A., Neiteler, R., Brussee, N., Makurat, A., Leu, L., Enzmann, F., Schwarz, J.O., Kersten, M., Irvine, S., Stampanoni, M.: Real-time 3d imaging of Haines jumps in porous media flow. Proceedings of the National Academy of Sciences of the United States of America **110**(10), 3755–3759 (2013)

[3] Bianchi, F., Thielmann, M., Mani, R.A., Or, D., Herrmann, H.J.: Tensile stress relaxation in unsaturated granular materials. Granular Matter **18**(4), 75 (2016)

[4] Blake, T.D., Ruschak, K.J.: Wetting: Static and Dynamic Contact Lines. In: Liquid Film Coating, pp. 63–97. Springer, Dordrecht (1997)

[5] Brakke, K.A.: The surface evolver and the stability of liquid surfaces. Philosophical Transaction of the Royal Society London A **354**, 2143–2157 (1996)

[6] Brendel, L., Unger, T., Wolf, D.E.: Contact Dynamics for Beginners. In: H. Hinrichsen, D.E. Wolf (eds.) The Physics of Granular Media, Wiley Online Books (2005)

[7] Bryant, S., Blunt, M.: Prediction of relative permeability in simple porous media. Physical Review A **46**(4), 2004–2011 (1992)

[8] Campbell, C.S.: Self-diffusion in granular shear flows. Journal of Fluid Mechanics **348**, 85101 (1997)

[9] Carr, J.F.: Tensile Strength of Granular Materials. Nature **213**(5081), 1158–1159 (1967)

[10] Coles, M.E., Hazlett, R.D., Spanne, P., Soll, W.E., Muegge, E.L., Jones, K.W.: Pore level imaging of fluid transport using synchrotron X-ray microtomography. Journal of Petroleum Science and Engineering **19**(1), 55–63 (1998)

[11] Cundall, P.A., Strack, O.D.L.: A discrete numerical model for granular assemblies. Géotechnique **29**(18), 47–65 (1979)

[12] Dijksman, J.A., van Hecke, M.: Granular flows in split-bottom geometries. Soft Matter **6**(13), 2901–2907 (2010)

[13] Feder, J.: Random sequential adsorption. Journal of Theoretical Biology **87**(2), 237–254 (1980)

[14] Fisher, R.A.: On the capillary forces in an ideal soil; correction of formulae given by W. B. Haines. The Journal of Agricultural Science **16**(3), 492505 (1926)

[15] de Gennes, P.G., Brochard-Wyart, F., Quere, D.: Capillarity and Wetting Phenomena: Drops, Bubbles, Pearls, Waves. Springer-Verlag, New York (2004)

[16] German, R.M.: Coordination number changes during powder densification. Powder Technology **253**, 368–376 (2014)

[17] Gladkikh, M.: A priori prediction of macroscopic properties of sedimentary rocks containing two immiscible fluids. Ph.D. thesis, University of Texas at Austin (2005)

[18] Gröger, T., Tüzün, U., Heyes, D.M.: Modelling and measuring of cohesion in wet granular materials. Powder Technology **133**(1), 203–215 (2003)
[19] Haines, W.B.: Studies in the physical properties of soils: II. A note on the cohesion developed by capillary forces in an ideal soil. The Journal of Agricultural Science **15**(04), 529–535 (1925)
[20] Haines, W.B.: Studies in the physical properties of soils: Iv. a further contribution to the theory of capillary phenomena in soil. The Journal of Agricultural Science **17**(2), 264–290 (1927)
[21] Halsey, T.C., Levine, A.J.: How Sandcastles Fall. Physical Review Letters **80**(14), 3141–3144 (1998)
[22] Hartley, R.R., Behringer, R.P.: Logarithmic rate dependence of force networks in sheared granular materials. Nature **421**(6926), 928–931 (2003)
[23] Herminghaus, S.: Dynamics of wet granular matter. Advances in Physics **54**(3), 221–261 (2005)
[24] Herrmann, H., Luding, S.: Modeling granular media on the computer. Continuum Mech Therm **10**(4), 189–231 (1998)
[25] Hornbaker, D.J., Albert, R., Albert, I., Barabási, A.L., Schiffer, P.: What keeps sandcastles standing? Nature **387**(6635), 765 (1997)
[26] Iveson, S.M., Litster, J.D., Hapgood, K., Ennis, B.J.: Nucleation, growth and breakage phenomena in agitated wet granulation processes: a review. Powder Technology **117**(1), 3–39 (2001)
[27] Kadau, D., Schwesig, D., Theuerkauf, J., Wolf, D.: Influence of particle elasticity in shear testers. Granular Matter **8**, 35–40 (2006)
[28] Kohonen, M.M., Geromichalos, D., Scheel, M., Schier, C., Herminghaus, S.: On capillary bridges in wet granular materials. Physica A: Statistical Mechanics and its Applications **339**(1), 7–15 (2004)
[29] Kohonen, M.M., Maeda, N., Christenson, H.K.: Kinetics of capillary condensation in a nanoscale pore. Physical Review Letters **82**, 4667–4670 (1999)
[30] Lambert, P., Chau, A., Delchambre, A., Régnier, S.: Comparison between two capillary forces models. Langmuir **24**(7), 3157–3163 (2008)
[31] Lian, G., Seville, J.: The capillary bridge between two spheres: New closed-form equations in a two century old problem. Advances in Colloid and Interface Science **227**, 53–62 (2016)
[32] Lian, G., Thornton, C., Adams, M.J.: A theoretical study of the liquid bridge forces between two rigid spherical bodies. Journal of Colloid and Interface Science **161**(1), 138–147 (1993)
[33] Lu, N., Wu, B., Tan, C.P.: Tensile strength characteristics of unsaturated sands. Journal of Geotechnical and Geoenvironmental Engineering **133**(2), 144–154 (2007)
[34] Lukyanov, A.V., Sushchikh, M.M., Baines, M.J., Theofanous, T.G.: Superfast Nonlinear Diffusion: Capillary Transport in Particulate Porous Media. Physical Review Letters **109**(21), 214,501 (2012)
[35] Mani, R.A.: Capillary interactions, shear thickening and liquid migration in wet granular media. Ph.D. thesis, ETH-Zürich (2014)

[36] Mani, R.A., Kadau, D., Herrmann, H.J.: Liquid migration in sheared unsaturated granular media. Granular Matter **15**(4), 447–454 (2013)
[37] Mani, R.A., Kadau, D., Or, D., Herrmann, H.J.: Fluid Depletion in Shear Bands. Physical Review Letters **109**(24), 248,001 (2012)
[38] Mani, R.A., Semprebon, C., Kadau, D., Herrmann, H.J., Brinkmann, M., Herminghaus, S.: Role of contact-angle hysteresis for fluid transport in wet granular matter. Physical Review E **91**(4), 042,204 (2015)
[39] Mason, G., Clark, W.: Tensile Strength of Wet Granular Materials. Nature **219**(5150), 149–150 (1968)
[40] Mellor, D.W.: Random close packing (rcp) of equal spheres: Structure and implications for use as a model porous medium. Ph.D. thesis, Open University, Milton Keynes, U.K. (1989)
[41] Melnikov, K.: Grain Scale Modelling of Triggering Mechanisms of Rainfall Induced Slope Failures. Ph.D. thesis, ETH Zürich (2016)
[42] Melnikov, K., Mani, R.A., Wittel, F.K., Thielmann, M., Herrmann, H.J.: Grain-scale modeling of arbitrary fluid saturation in random packings. Physical Review E **92**(2), 022,206 (2015)
[43] Melnikov, K., Wittel, F.K., Herrmann, H.J.: Micro-mechanical failure analysis of wet granular matter. Acta Geotechnica **11**(3), 539–548 (2016)
[44] Melrose, J.C.: Wettability as Related to Capillary Action in Porous Media. Society of Petroleum Engineers Journal **5**(03), 259–271 (1965)
[45] Mitarai, N., Nori, F.: Wet granular materials. Advances in Physics **55**(1), 1–45 (2006)
[46] Moreau, J.J.: Some numerical methods in multibody dynamics: application to granular materials. European Journal of Mechanics A - Solids **13**, 93–114 (1994)
[47] Morrow, N., Mason, G.: Recovery of oil by spontaneous imbibition. Current Opinion in Colloid And Interface Science **6**(4), 321–337 (2001)
[48] Motealleh, S., Ashouripashaki, M., DiCarlo D. Bryant, S.: Unified model of drainage and imbibition in 3d fractionally wet porous media. Transport in Porous Media **99**(3), 581–611 (2013)
[49] Pierrat, P., Agrawal, D.K., Caram, H.S.: Effect of moisture on the yield locus of granular materials: theory of shift. Powder Technology **99**(3), 220–227 (1998)
[50] Pierrat, P., Caram, H.S.: Tensile strength of wet granular materials. Powder Technology **91**(2), 83–93 (1997)
[51] Richefeu, V., El Youssoufi, M.S., Radjaï, F.: Shear strength properties of wet granular materials. Physical Review E **73**(5), 051,304 (2006)
[52] Rognon, P.G., Roux, J.N., Wolf, D., Naaïm, M., Chevoir, F.: Rheophysics of cohesive granular materials. EPL (Europhysics Letters) **74**(4), 644 (2006)
[53] Rynhart, P., McLachlan, R., Jones, J., McKibbin, R.: Solution of the young-laplace equation for three particles. Research Letters in the Information and Mathematical Sciences **5**(4), 119–127 (2003)
[54] Sanders, C.: An open source C++ linear algebra library for fast prototyping and computationally intensive experiments. Tech. rep., NICTA (2010)

[55] Scheel, J., Seemann, R., Brinkmann, M., Di Michiel, M., Sheppard, A., Breidenbach, B., Herminghaus, S.: Morphological clues to wet granular pile stability. Nature Materials **7**(3), 189–193 (2008)
[56] Scheel, J., Seemann, R., Brinkmann, M., Di Michiel, M., Sheppard, A., Herminghaus, S.: Liquid distribution and cohesion in wet granular assemblies beyond the capillary bridge regime. Journal of Physics, Condensed Matter **20**(49), 494,236 (2008)
[57] Scheel, M.: Experimental investigations of the mechanical properties of wet granular matter. Ph.D. thesis, Georg-August-Universität Goettingen (2009)
[58] Scholtès, L.: Modélisation micromécanique des milieux granulaires partiellement saturés. Ph.D. thesis, Institut National Polytechnique de Grenoble - INPG (2008)
[59] Scholtès, L., Chareyre, B., Nicot, F., Darve, F.: Micromechanics of granular materials with capillary effects. International Journal of Engineering Science **47**(1), 64–75 (2009)
[60] Scholtès, L., Hicher, P.Y., Nicot, F., Chareyre, B., Darve, F.: On the capillary stress tensor in wet granular materials. International Journal for Numerical and Analytical Methods in Geomechanics **33**(10), 1289–1313 (2009)
[61] Seemann, R., Mönch, W., Herminghaus, S.: Liquid flow in wetting layers on rough substrates. EPL (Europhysics Letters) **55**(5), 698–704 (2001)
[62] Semprebon, C., Scheel, M., Herminghaus, S., Seemann, R., Brinkmann, M.: Liquid morphologies and capillary forces between three spherical beads. Physical Review E **94**, 012,907 (2016)
[63] Shi, D., McCarthy, J.J.: Numerical simulation of liquid transfer between particles. Powder Technology **184**(1), 64–75 (2008)
[64] Tsunakawa, H., Aoki, R.: Tensile strength of wet granular materials. Chemical engineering **36**(3), 281–286,a1 (1972)
[65] Ulrich, S., Aspelmeier, T., Zippelius, A., Roeller, K., Fingerle, A., Herminghaus, S.: Dilute wet granular particles: Nonequilibrium dynamics and structure formation. Physical Review E **80**(3), 031,306 (2009)
[66] Utter, B., Behringer, R.P.: Self-diffusion in dense granular shear flows. Physical Review E **69**, 031,308 (2004)
[67] Vogel, H.J., Roth, K.: Quantitative morphology and network representation of soil pore structure. Advances in Water Resources **24**(3), 233–242 (2001)
[68] Wang Qiong, Lade Poul V.: Shear Banding in True Triaxial Tests and Its Effect on Failure in Sand. Journal of Engineering Mechanics **127**(8), 754–761 (2001)
[69] Widom, B.: Capillarity and Wetting Phenomena: Drops, Bubbles, Pearls, Waves. Physics Today **57**(12), 66–67 (2004)
[70] Willett, C.D., Adams, M.J., Johnson, S.A., Seville, J.P.K.: Capillary bridges between two spherical bodies. Langmuir **16**(24), 9396–9405 (2000)
[71] Zhou, T., Ioannidou, K., Masoero, E., Mirzadeh, M., Pellenq, R.J.M., Bazant, M.Z.: Capillary stress and structural relaxation in moist granular materials. under review by Physical Review Letters p. 6 (2018). https://arxiv.org/abs/1803.05879